bioRxiv

Long-term stability of avalanche scaling and integrative network organization in prefrontal and premotor cortex

Stephanie R. Miller[1], Shan Yu[1,2], Sinisa Pajevic[3], and Dietmar Plenz[1]

[1] Section on Critical Brain Dynamics, National Institute of Mental Health, Bethesda, MD, USA.

[2]Current address: Brainnetome Center, Institute of Automation, Chinese Academy of Sciences, China.

[3]Section on Quantitative Imaging and Tissue Sciences, National Institute of Child Health and Development, NIH, Bethesda, MD, USA.

Pages/Figures: 6 figures, 4 tables

Running Head: Long-term stability in avalanches and functional networks

Correspondence: Dietmar Plenz, Ph.D., Section on Critical Brain Dynamics, National Institute of Mental Health, Porter Neuroscience Research Center, Rm 3A-1000, 35 Convent Drive, Bethesda, MD 20892, (301) 402-2249 office, (301) 480-7480 fax, plenzd@mail.nih.gov

Keywords: nonhuman primate, resting activity, criticality, brain dynamics, neuronal avalanches, integrative network organization

Abstract

Ongoing neuronal activity in the brain establishes functional networks that reflect normal and pathological brain function. Most estimates of these functional networks suffer from low spatiotemporal resolution and indirect measures of neuronal population activity, limiting the accuracy and reliability in their reconstruction over time. Here, we studied the stability of neuronal avalanche dynamics and corresponding reconstructed functional networks in the adult brain. Using chronically implanted high-density microelectrode arrays, the local field potential (LFP) of resting state activity was recorded in prefrontal and premotor cortex of awake nonhuman primates. Avalanche dynamics revealed stable scaling exhibiting an inverted parabolic profile and collapse exponent of 2 in line with a critical branching process over many days and weeks. Functional networks were based on a Bayesian-derived estimator and demonstrated stable integrative properties characterized by non-trivial high neighborhood overlap between strongly connected nodes and robustness to weak link pruning. Entropy-based mixing analysis revealed significant changes in strong link weights over weeks. The long-term stability in avalanche scaling and integrative network organization in the face of individual link weight changes should support the development of non-invasive biomarkers to characterize normal and abnormal brain states in the adult brain.

18 # Introduction

19 Ongoing neuronal activity in the mammalian brain gives rise to distinct functional networks that
20 reflect normal and pathological brain function (Bullmore and Sporns, 2009; Fox and Raichle,
21 2007; Raichle, 2015). Empirical measures of these networks, however, are often limited in the
22 precision with which they reflect the organization of neuronal population activity. Networks are
23 either reconstructed from indirect non-neuronal activity at low temporal resolution using
24 functional magnetic resonance imaging (fMRI), while more direct neuronal activity measures
25 such as magnetoencephalography (MEG) and the electroencephalogram (EEG) suffer
26 predominantly from low spatial resolution (Bassett and Sporns, 2017). Accordingly, there is
27 limited knowledge about the spatiotemporal dynamics and corresponding functional connectivity
28 of local neuronal populations giving rise to fluctuations in ongoing cortical activity.

29 Neuronal activity measured at single cell resolution could in principle allow for precise
30 spatiotemporal reconstruction of functional networks in cortex. For example, in macaque cortex
31 single-unit activity can be recorded over many weeks (Nicolelis et al., 2003) and identifies firing
32 statistics of neurons over days (Dickey et al., 2009; Jackson and Fetz, 2007). Advanced
33 approaches may involve tetrodes, automated classifiers (Tolias et al., 2007) or second order
34 statistics as classifiers (Fraser and Schwartz, 2011). Even advanced single-unit approaches,
35 however, limit robust tracking of activity to small groups of individual neurons. Chronic
36 expression of genetically-encoded calcium indicators (GECIs) can increase the neuronal count
37 and identify orientation selective neurons over months (Li et al., 2017), yet at low temporal
38 resolution. The local field potential (LFP), alternatively, provides access to an intermediate
39 spatial resolution of cortical activity that is between the macroscopic scale of fMRI, MEG and
40 EEG and single cell accuracy. It robustly measures local neuronal population activity with high

temporal and reasonable spatial resolution of several hundred micrometers. In nonhuman primates, the LFP has been shown to correlate well with local unit-activity (Donoghue et al., 1998; Petermann et al., 2009; Rasch et al., 2008) and offers robust brain-machine interface performance (Mehring et al., 2003).

It is now well established that the ongoing LFP in superficial layers of nonhuman primates organizes into spatiotemporal activity clusters whose sizes and durations distribute according to power laws (Miller et al., 2019; Shew et al., 2009; Yu et al., 2017), the hallmark of neuronal avalanches (Beggs and Plenz, 2003). The spatiotemporal correlations underlying neuronal avalanches give rise to functional 'integrative' networks, such that nodes with strong connections are likely to have many common neighbors and are robust against pruning of weak links (Pajevic and Plenz, 2012). However, the stability over days and weeks of cortical avalanche dynamics and corresponding integrative networks is currently not known. Size and duration distributions do not consider the spatiotemporal organization of avalanches, thus multiple functional connectivities could give rise to similar power law statistics. Likewise, integrative networks allow for pairwise changes while maintaining global integrative properties (Pajevic and Plenz, 2012).

Here we recorded ongoing LFP activity in prefrontal and premotor areas of the macaque brain over weeks using chronically implanted high-density microelectrode arrays. We demonstrate stable avalanche dynamics with power law statistics, parabolic temporal profiles and a size-vs-duration scaling exponent of 2 in support of critical branching process dynamics (Friedman et al., 2012; Miller et al., 2019; Sethna et al., 2001). We further demonstrate that these avalanches give rise to non-trivial integrative functional networks despite progressive changes in

strong link strength as identified using normalized-count (NC) estimators (Pajevic and Plenz, 2009). Our results suggest avalanche dynamics and corresponding integrative networks to identify a robust cortical state in the adult brain, which might allow for the early identification of deviations towards pathological brain states.

Results

The spatiotemporal organization of the ongoing LFP (1 – 100 Hz) was monitored with chronically implanted high-density microelectrode arrays (~10 x 10 electrodes; interelectrode distance 400 μm) in premotor (PM, n = 2 arrays) and prefrontal cortex (PF, n = 4 arrays) of three nonhuman primates (*Macaca mulatta*; K, V, N; Fig. 1A, B). The animals were awake and seated in a monkey chair during the recording sessions but were not given any specific stimulus or task. About 4 ± 2 hr of activity were analyzed during 9 ± 7 recording sessions over the course of 5 ± 4 weeks (85 ± 8 electrodes/array; Fig. 1C).

Stability of average pairwise correlation and avalanche dynamics in prefrontal and premotor cortex

The pairwise Pearson's correlation, R, is a standard measure to quantify the correlation in neuronal activity between distant cortical sites. We found that for the continuous LFP, the distribution of R, obtained from ~5,000 electrode comparisons per array, was broad yet similar across days (Fig. 1D, E). The average correlation, <R>, while different between arrays, was constant over many days and weeks (Fig. 1F, G; linear regression fit of $0.4 \pm 0.7 \times 10^{-2}$ for all arrays; see Table 1 for individual arrays).

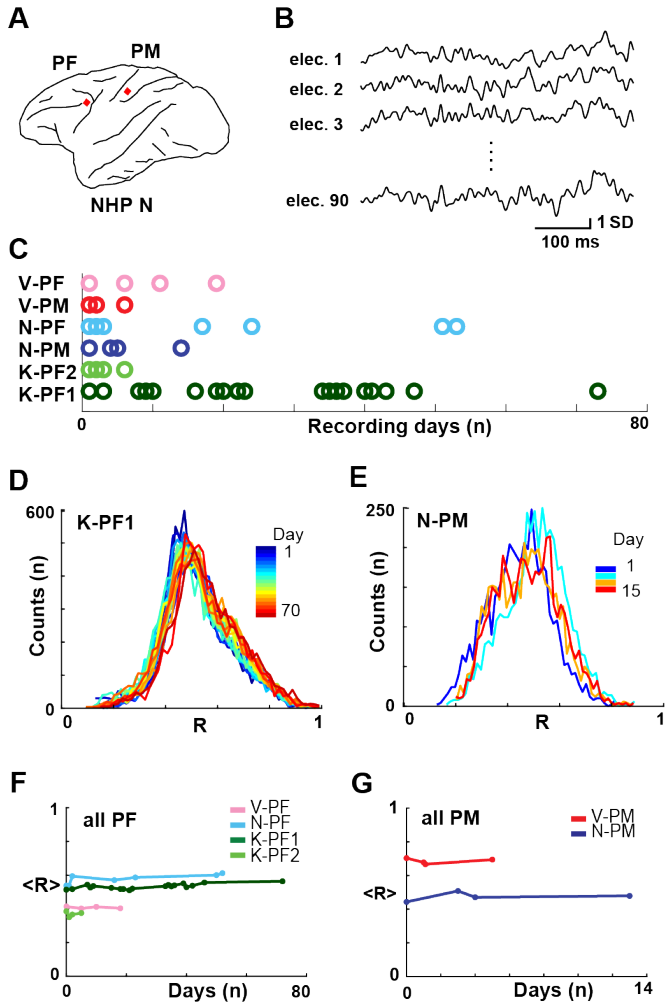

Figure 1: Ongoing cortical dynamics are stable over weeks in superficial layers assessed by pairwise correlations in the LFP. A, Sketch of chronic prefrontal (PF) and premotor (PM) implantation sites for high-density microelectrode arrays. **B,** Example of simultaneously recorded ongoing LFP (1 – 100 Hz) at single electrodes with correlated activity at various time scales. **C,** Overview of ~30 min recording sessions over several weeks for each NHP. **D, E,** Pair-wise correlations distribute similar over time. Normalized histogram of pairwise correlations between all functioning channels for each recording day (*color bar*) in two subjects (*left*: prefrontal recording in NHP K; *right*: premotor recordings in NHP N). **F, G**, The average correlation, <R> (from D, E), was stable over weeks in prefrontal (*left*) and premotor arrays (*right*).

83

We next explored the stability of neuronal avalanche dynamics described previously for ongoing LFP activity in nonhuman primates (Petermann et al., 2009; Yu et al., 2017). Discrete LFP events were defined as negative deflections in the LFP at each electrode (Fig. 2A) crossing a threshold of -2 SD and grouped into avalanches at temporal resolution Δt of the mean interevent interval, <IEI>, which ranged between 3 – 4 ms (Fig. 2B; see Material and Methods). We found that the probability density distribution of avalanche size, which ranged from size 1 to the number of electrodes for each array, exhibited power laws for each day of recording (Fig. 2C, D; Δt = <IEI>, truncated power law vs. exponential, LLR >> 1, $P < 0.005$; or vs. log-normal, LLR>>1, $P < 0.005$; constant across all recording days). The stability of the power law in size was associated with a slope α of 1.32 ± 0.05 for all arrays (see also Table 1), which is close to the expectations for the size exponent of a critical branching process (Fig. 2E, F) (Harris, 1963). These results demonstrate the presence of avalanche dynamics in all subjects for up to 2 weeks in PM and up to 10 weeks in PFC.

Long-term stability in the temporal profile of avalanches and corresponding scaling collapse

The temporal profile of a neuronal avalanche describes how avalanches unfold in time by initiating locally, growing in magnitude, and eventually contracting spatially before ending. Recent work (Miller et al., 2019) confirmed that the temporal profile of neuronal avalanches obeys the characteristic motif of an inverted parabola and that empirically observed mean avalanche profiles collapse onto this motif regardless of avalanche duration. For this analysis, the temporal resolutions were set to 1 ms and 30 ms respectively. These resolutions allow the

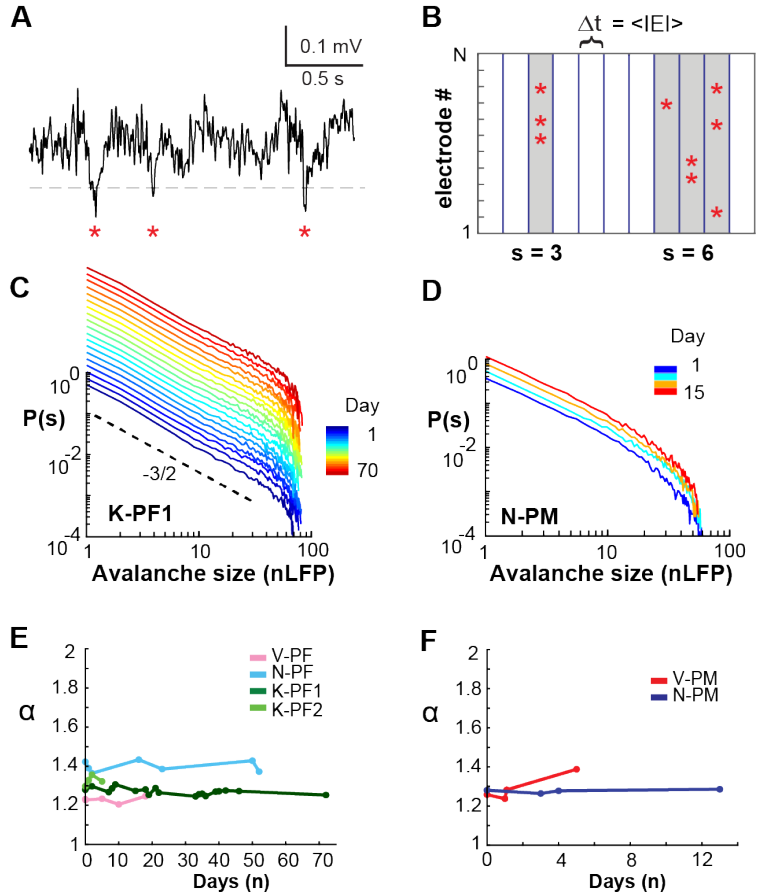

Figure 2: Ongoing neuronal avalanche activity is stable over weeks in superficial cortical layers. A, Sample ongoing LFP at single electrode. A negative threshold (*dashed line*) is applied to identify significant negative deflections from the mean (nLFPs, *red asterisks*). **B,** Schematic activity raster showing neuronal avalanches identified as concurrent or consecutive nLFPs on the array separated by at least one empty time bin. **C, D,** Power law distributions in nLFP cluster size identifies avalanche dynamics for all recordings (*color bar*) in two subjects (Δt = ⟨IEI⟩). *Broken line*: power law with slope -3/2. *Color bar*: Recording day. Size distributions remain power laws for all days (LLR values > 0 significant; vs. exponential distribution). **E, F,** Stability of slope α as a function of time (*color coded*).

collapse of temporal avalanche profiles in the presence of transient γ–oscillations characteristic of cortical activity in resting NHP (Miller et al., 2019) in the presence of stable size distributions power laws (Table 1; 1 ms: all LLR > 10^4, all $p << 0.005$; 30ms: all LLR > 10, all $p << 0.005$).

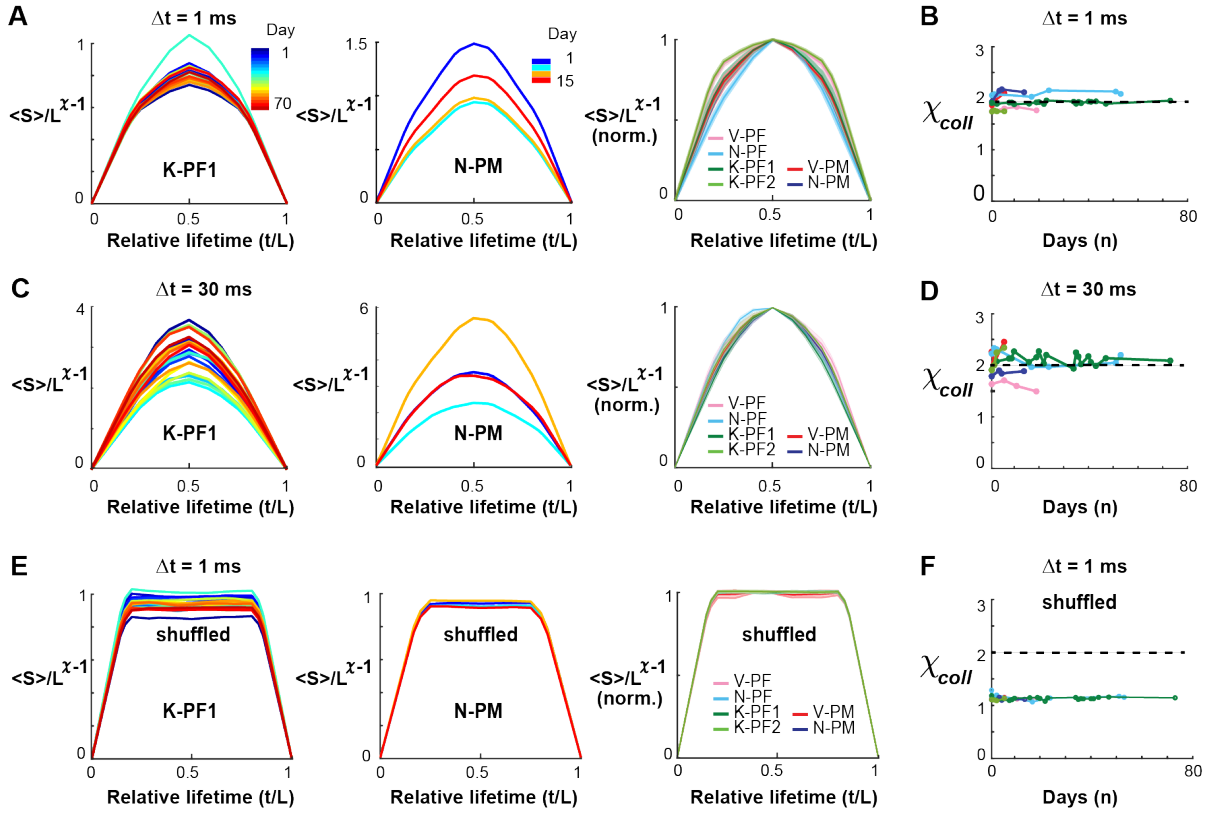

Figure 3: Renormalization collapse of neuronal avalanche temporal profiles and scaling exponent χ = 2 are stable over weeks in superficial layers. A, Collapse in the temporal profile of avalanches at Δt = 1 ms. Individual recording days for K-PF1 (*left*) and N-PM (*middle*) for all days (*color bar*) showing the best collapse for each day. Summary of normalized collapse motif averaged across days for each NHP and cortical area (*right*), mean ± s.e.. **B,** The scaling exponent χ at which the best temporal profile collapse is obtained remains close to the theoretical value of 2 predicted for a critical branching process (Harris, 1963) for all recording sessions. **C, D** Same as in *A*, *B* but at Δt = 30 ms demonstrating the characteristic parabolic profile for coarse-grained temporal scale. **E**, Same as in *A-D*, but nLFP events have been shuffled in time to remove temporal correlations. Note that the characteristic profile no longer traces a parabola as expected for critical dynamics. **G**, The scaling exponent χ is close to 1 in line with expectations for non-critical dynamics (e.g. (Sethna et al., 2001; Villegas et al., 2019).

We explored the stability of these predictions of avalanche profiles over time, finding that the characteristic motif for mean profiles of avalanche durations L = 3Δt – 5Δt did trace inverted parabolas for fine (Δt = 1 ms, Fig. 3A, B,) and coarse (Δt = 30 ms, Fig. 3C, D) temporal

resolutions (for statistical comparison see Table 2 for individual arrays). Importantly, the scaling exponent χ producing these parabolic, collapsed motifs was close to the value of 2 expected for a critical branching process (Harris, 1963; Sethna et al., 2001) and did not change over time (Fig. 3B, D; for $\Delta t = 1$ ms, $\chi = 1.93 \pm 0.14$, linear regression fit of $1*10^{-2} \pm 0.2$; for $\Delta t = 30$ ms, $\chi = 2.01 \pm 0.24$, linear regression slope of $2*10^{-2} \pm 0.04$; Table 3 for individual arrays). In contrast, time-shuffled data reliably produced flattened motifs (Fig. 3E, F) with a scaling exponent close to 1, in agreement with predictions for non-critical dynamics, in which sizes simply grow linearly with duration (Villegas et al., 2019).

Persistence of integrative global network properties

In order to quantify in more detail the spatiotemporal correlations underlying persistent avalanche activity, we reconstructed functional networks from neuronal avalanches solely using the Normalized Count method (Pajevic and Plenz, 2009). This method uses a shortcut to Bayesian estimation of network connections, making it approximate but also computationally efficient, and hence applicable to reconstructing relatively large networks from lengthy event train recordings (Fig. 4A). It also reduces the influence of indirect common input correlations and has been found in simulations to accurately and efficiently reconstruct the directed networks and weights from simulated point process dynamics (Pajevic and Plenz, 2009). An example of the directed connectivity matrix for a single recording session derived from spontaneous avalanche activity is shown in Figure 4B. We found that for all arrays and recording sessions, the weights of the directed functional connections were not particularly heavy-tailed and distributed between an exponential and lognormal function over more than 3 orders of magnitude (Fig. 4C – E).

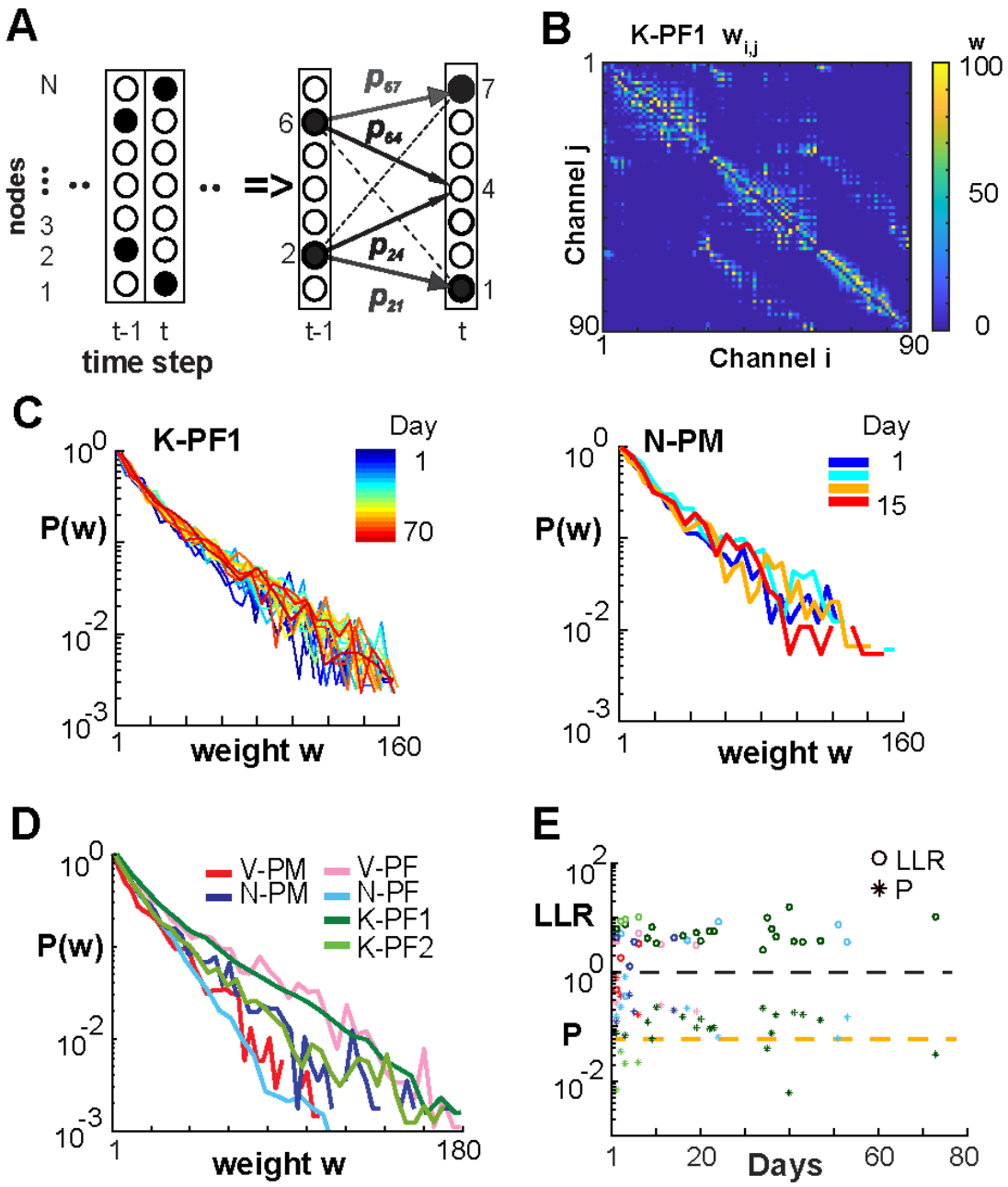

Figure 4: Normalized Count reconstruction of directed functional connectivity from ongoing LFPs reveals stable exponential distributions in links across time for all NHPs. A, Normalized Count reconstructed network based on 30 minutes of LFP activity from N-PM produces an adjacency matrix showing sparse, mostly local functional connectivity. **B**, Example of a Normalized Count reconstructed directed functional connectivity matrix from a single experimental recording (K-PF1). **C,** Normalized distributions in directed link strength for all recording days (*left*, K-PF1; *right*, Nom-PM). *Color bar*: recording day). **D,** Normalized probability distribution trends were consistent across areas and subjects. Average distribution over all recording days. *Color code*: NHP-area. **E**, LLR (open circle) and P values (star) for exponential vs. lognormal comparison of daily weight distributions (e.g. C) for all arrays and days (color code as in D).

Having reconstructed the directed weights in our avalanche-derived functional connectivity, we proceeded to calculate several graph theoretical properties. Integrative networks are characterized by a positive correlation, R, between the link cluster coefficient, C_L, and the corresponding link weight, w, between two nodes (Fig. 5A; (Pajevic and Plenz, 2012)). This positive correlation demonstrates that more strongly connected nodes have more common neighbors compared to weakly connected nodes (Fig. 5B). We employed degree-sequence preserved randomization to subtract potential contributions to link clustering from the node degree distribution and report here the resulting excess link clustering, ΔC_L (see Material and Methods). The monotonic increase in ΔC_L with lowest-to-highest weight rank clearly identifies avalanche dynamics in both PM and PFC to emerge from an integrative functional network organization (Fig. 5C) that was stable over time (Fig. 5D; linear regression slope of $5 \pm 10 \times 10^{-3}$; 95% confidence limit; see Table 4 for individual arrays).

Pruning analysis is an efficient approach to study the weight-dependent internal organization of networks (Onnela et al., 2007; Pajevic and Plenz, 2009). We found that pruning from the bottom, i.e. pruning weakest links progressively, had negligible effect on the network clustering properties. This was evidenced by a near constant value of ΔC_L until the vast majority (80 – 90%, Fig. 5E; solid lines) of links were removed. In contrast, pruning from the top, i.e. removing the strongest links first, rapidly decreased ΔC_L, a result consistently found for all subjects (Fig. 5E; broken lines). We conclude that the integrative property arises from a 'backbone' of strong links that is robust to weak-link-pruning, yet quickly degrades when strong links are removed.

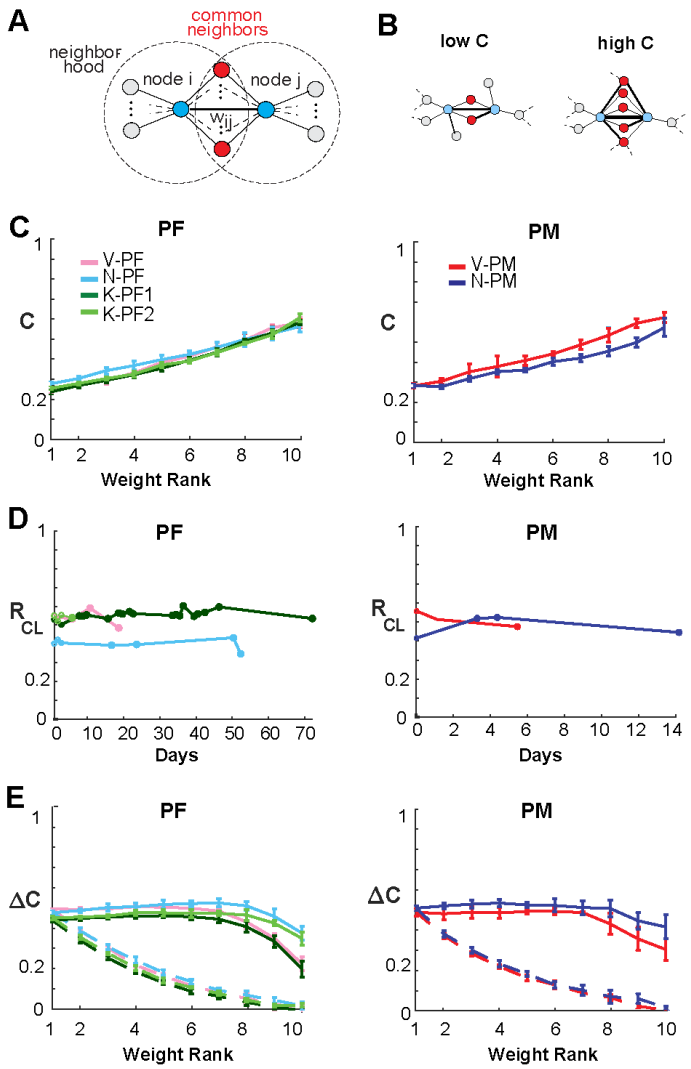

Figure 5: Link-clustering analysis reveals that integrative global network properties are stable over time. A, Schematic clustering diagram depicting two nodes (*blue*) connected by a link with weight w_{ij}. In an integrative network, the proportion of common neighbors (*red*) is expected to positively correlate with w_{ij}. **B,** Sketch of two subnetworks with low and high link clustering C respectively. **C,** Clustering increased with link strength in all prefrontal (*left*) and premotor (*right*) cortical arrays (*color coded*; NHP-area). **D,** Analysis of cortical networks showed strongly positive R_{CL} over all recording sessions for up to 73 days. **E,** Link-pruning analysis of excess clustering ΔC calculated via degree sequence preserved randomization (DSPR) (Pajevic and Plenz, 2012) showed that the integrative clustering motif was robust to weak-link-pruning (*solid lines*; error bars denote mean ± SD over all recordings for an array), while the clustering 'backbone' of the network quickly degraded when strong links were pruned first (*dotted lines*; reverse weight rank on the lower axis; *color code* as in D). C – E, Δt = 1 ms.

155

Persistence of link hierarchy over many weeks

Given the stability observed over weeks in the average pairwise correlation, power law exponent, avalanche scaling and integrative network organization, we analyzed in more detail the stability of individual link weights. Two major factors contribute to potential fluctuations in link weights in a network. First, imprecision in network reconstruction, which will result in a constant mixing term for any pairwise comparison in time. Second, link weights could gradually change over days and weeks, which is progressive and therefore is expected to lead to a monotonic increase in mixing entropy H_M until maximal mixing is reached. Alternatively, links could change randomly from day to day at which point H_M quickly reaches the maximal attainable entropy for link randomization. We quantified potential changes in link weight from NC reconstructed networks for the upper half (top 50%) and lower half (bottom 50%) separately, in line with our results for top- vs. bottom pruning results demonstrating differences in network robustness to link changes in the top or bottom half of the link weight distribution. For each half, we partitioned link weights further into strength quintiles and then studied whether members from different quintiles will mix over time. In the plots in Figure 6, we show the data for the "top" (black curve) and "bottom" (green curve) and compare those curves to H_M obtained if the labels were fully randomized at each step (dashed lines of the same color). We also show the theoretical maximum for H_M (red dashed line). Because all successive distributions were using the link labels derived from Day 1 (making $H_M = 0$), the average entropy of mixing was plotted beginning at the second recording for each subject. For all arrays, we found that H_M reaches close to the maximal entropy within the next day demonstrating that weak links fluctuate randomly. On the other hand, we found progressive and significant increases of H_M over days for strong links in three out of six arrays (Figure 6A,B). These findings demonstrate stability in

avalanche dynamics and integrative network organization even when strong links demonstrate progressive weight changes at the individual link level.

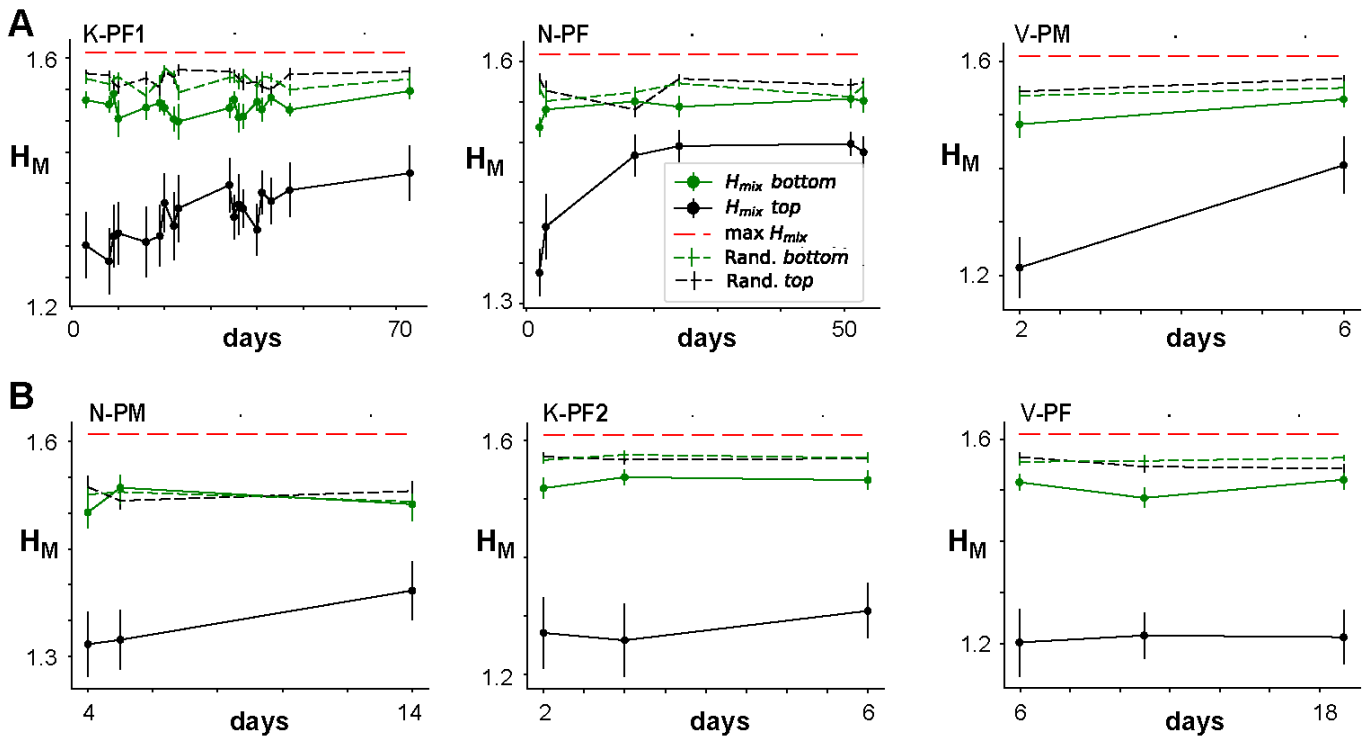

Figure 6: Entropy of mixing analysis of the network link weight fluctuations over many days. Entropy of mixing (H_M) analysis of the link weights obtained with normalized count (NC) reconstructions from Δt = 1 ms raster recordings. H_M is plotted for the "top" (strongest 50% of links; black curves) and "bottom" (weakest 50% of links; green curves) versus the days after the initial recording. The black and green dashed lines indicate corresponding H_M obtained when the labels were fully randomized, while the red dashed line indicate the theoretical maximum. The six panels represent six different monkeys, shown in two rows. **A**, Arrays for which statistically significant progression of mixing was obtained for "top" links; row. **B**, Arrays for which no statistically significant progression was observed. The "top" half of the links was always yielding lower H_M than the "bottom" half of the links, which is mainly due to the smaller reconstruction error. The Day 1 points are not plotted as by default of our labeling the value for H_M is zero.

Discussion

Here we recorded the ongoing LFP activity in prefrontal and premotor areas of the macaque brain over weeks using chronically implanted high-density microelectrode arrays. We demonstrate stable avalanche dynamics with power law statistics, parabolic temporal profiles and a scaling exponent of 2 in support of critical branching process dynamics (Friedman et al., 2012; Miller et al., 2019; Sethna et al., 2001). We further demonstrate that these avalanches form integrative networks with progressive change in individual link weights as identified using NC estimators and entropy mixing approach (Pajevic and Plenz, 2009). Our results suggest avalanche dynamics and corresponding integrative networks to identify a robust state of the awake frontal cortex in the face of changes between individual cortical sites. This work is impactful for computational studies of frontal cortex function and translational research into the quantification of abnormal cortex states as encountered e.g. in mental diseases.

Our long-term analysis was based on high-density recordings of the ongoing LFP. While there have been technical advances in identifying long-term robustness in neuronal activity using cellular resolution approaches (Dickey et al., 2009; Fraser and Schwartz, 2011; Jackson and Fetz, 2007; Li et al., 2017; Nicolelis et al., 2003; Tolias et al., 2007), cellular approaches suffer from spatial subsampling (Levina and Priesemann, 2017; Petermann et al., 2009; Ribeiro et al., 2010; Ribeiro et al., 2014) preventing proper identification of avalanche dynamics and corresponding reconstruction of functional connectivity. The LFP, particularly when recorded from superficial layers, is a robust signal carrying local population activity that contains local spike information (Donoghue et al., 1998; Mehring et al., 2003; Petermann et al., 2009; Rasch et al., 2008). Yet, the cellular circuits contributing to the LFP cannot be resolved unambiguously, limiting insight

into how the robustness in avalanche dynamics and link weight organization is achieved in the brain over days and weeks.

Experiments and simulations have provided insights into the ability of cortical networks to maintain avalanche dynamics. Prolonged perturbation in the excitation/inhibition balance through pharmacological means *in vitro* cortex cultures (Plenz, 2012) and sensory deprivation *in vivo* visual cortex (Ma et al., 2019) abolish avalanche dynamics initially. Yet, microcircuits recover over the course of several days suggesting the presence of homeostatic mechanisms in cortex to maintain avalanche dynamics. Early in development, neuronal avalanches emerge autonomously in isolated cortex *in vitro* around the time superficial layers develop (Stewart and Plenz, 2008; Tetzlaff et al., 2010). This emergence absent sensory input similarly points to a homeostatic regulation of avalanche dynamics in cortex. Neuronal simulations have identified a specific learning rule that operate on activity cascades such as avalanches, which implement integrative network weight organization (Pajevic and Plenz, 2012). Importantly, this rule emphasizes link changes at recent cascade failure locations which opens up network bottleneck's in the presence of avalanche dynamics (Alstott et al., 2015). Yet, the stability of avalanche dynamics and integrative network organization over many weeks in the adult brain *in vivo* had not been quantified. The present neuronal avalanche analysis consistently produced power law distributions in avalanche sizes and a scaling exponent of 2 in line with expectations from a critical branching process for the adult brain (Miller et al., 2019; Sethna et al., 2001).

The central mechanisms underlying homeostatic regulation of avalanche dynamics and functional network organization will require advanced techniques at cellular resolution suitable for long-term monitoring. Potential candidate techniques are ratiometric genetically encoded

calcium indicators that naturally compensate for cell-intrinsic expression variability (Lutcke et al., 2013). Similarly, precise perturbation approaches need to be employed to determine whether the observed stability in dynamics and functional connectivity underlies homeostatic regulation (Chialvo et al., 2020).

Our reconstructed functional networks were based on a Bayesian-derived Normalized Count (NC) approach, easily scalable to large networks (Pajevic and Plenz, 2009, 2012). The NC efficiently utilizes long timeseries from small and large networks to identify the directed, functional network in which correlations from common input are significantly reduced. Network simulations demonstrated ground-truth reconstruction for various small-world topologies from subcritical, supercritical and critical dynamics, the latter in line with avalanche activity (Pajevic and Plenz, 2009). The predominantly exponential or weakly lognormal decay in directed link weights demonstrates that strong links in frontal cortex networks are part of a continuous distribution and our shuffling controls demonstrate that the integrative organization cannot be simply explained by the link degree distribution. Furthermore, given the robustness of the NC approach to underlying dynamics and topologies, we suggest that the identification of stable integrative networks is not simply a consequence of critical branching process dynamics generating avalanches, which can be realized in many topologies and architectures. Future work at cellular resolution and controlled local perturbation will be required to understand the potential plasticity mechanisms that link critical brain dynamics and integrative networks (Alstott et al., 2015; Pajevic and Plenz, 2012). We note that integrative networks differ from networks in which the weight is positively correlated with the node degree (Barrat et al., 2004; Bianconi, 2005; Pajevic and Plenz, 2012).

Connectome analyses on a time scale of seconds have identified transient fluctuations in functional connectivity reflecting distinct states (Hutchison et al., 2013; Liu and Duyn, 2013; Zalesky et al., 2014), which based on computational modeling were found to be intermittent, a signature of metastability (Deco et al., 2017; Hansen et al., 2015). Short-term fluctuations in the face of long-term stability is a hallmark of critical dynamics, which operates in a fluctuation dominated state (Fraiman and Chialvo, 2012; Tagliazucchi et al., 2012). Our analysis of the link-weight hierarchy demonstrated that contributes to these insights over a longer time range. When observed over the course of weeks based on 12 – 60 min periods, weak individual links do not show any particular trend over time. However, in at least 3 of our recordings significant progression in the mixing of strong links was observed suggesting that integrative network organization remains stable even when strong links are changing.

Heterogeneous activity in the form of neuronal avalanches has been the hallmark of ongoing (Beggs and Plenz, 2003; Bellay et al., 2015) and evoked (Yu et al., 2017) brain activity in superficial layers of the cerebral cortex. The scale-invariant hallmark of avalanches has been found to capture ongoing neuronal activity in nonhuman primates at the mesoscopic level, i.e. the local field potential (LFP) (Klaus et al., 2011; Petermann et al., 2009; Yu et al., 2014; Yu et al., 2017; Yu et al., 2011) and macroscopic activity measured with EEG (Meisel et al., 2013), MEG (Shriki et al., 2013) and fMRI (Fraiman and Chialvo, 2012; Tagliazucchi et al., 2012). The power law distributions in cluster size and duration support the idea that the cortex operates close to a critical state (Gautam et al., 2015; Kinouchi and Copelli, 2006; Shew et al., 2009; Shew et al., 2011; Yang et al., 2012). Our demonstration of a scaling exponent of 2 and parabolic avalanche shape is in line with predictions that the unfolding of avalanches in the brain is governed by a critical branching process. Recently, avalanches with a scaling factor of 2 have

been described for whole brain neuronal activity in the zebrafish larvae (Ponce-Alvarez et al., 2018), however, the corresponding size and duration exponent was significantly steeper compared to reports for the mammalian cortex suggesting a different dynamical model for the zebrafish.

In conclusion, we found that ongoing population dynamics in the form of neuronal avalanches and emerging macroscopic network properties in the form of integrative networks persisted over days and weeks in the adult brain. We suggest our work has implications for studies of brain disorders characterized by altered neurological development on the network and population level, such that the observed changes in global network properties and dynamics could be attributed to disease phenotypes.

Material and Methods

Animal procedures. All animal procedures were conducted in accordance with NIH guidelines and were approved by the Animal Care and User Committee of the National Institute of Mental Health (NIMH; Protocol LSN-11). Three adult nonhuman primates (NHP; *Macaca mulatta*; 1 male, 2 females; 7–8 years old) received two chronic implantations of high-density 96-microelectrode arrays (Blackrock Microsystems; 4×4 mm^2; 400 µm interelectrode distance; 10×10 grid with corner grounds). To direct recordings towards superficial cortical layers II/III, electrode shanks of 0.6 mm length were used in prefrontal cortex (PF; n = 4), and shanks of 1 mm length were used for premotor cortex (PM; n = 2). During recording sessions monkeys sat head-fixed and alert in a monkey chair with no behavioral task given. Portions of this dataset have been analyzed previously (Meisel et al., 2013; Miller et al., 2019; Yang et al., 2012; Yu et al., 2014).

Local field potential recordings in awake monkeys. Simultaneous and continuous extracellular recordings were obtained for 12 – 60 min per recording session (2 kHz sampling frequency), band-pass filtered between 1 – 100 Hz (6th-order Butterworth filter) to obtain the local field potential (LFP), and notch-filtered (60 Hz) to remove line noise. About 2 ± 1% of time periods were removed from functional electrodes due to artifacts introduced by e.g. vocalization, chewing, sudden movements. These artifacts were identified by threshold crossing (SD > 7) and excised (± 0.25 s). Arrays on average contained 86 ± 8 functional electrodes that exhibited 64 ± 50 μV of spontaneous LFP fluctuations (SD). Channels which had been removed from any recording were discounted for all recordings. Electrode LFPs were z-transformed and recording sessions for each array were analyzed individually. The current study represents a combined 26 hr of ongoing cortical LFP activity.

Avalanche definition. For each electrode in the array, absolute peak amplitudes and times of negative LFP (nLFP) threshold crossings (–2 SD) were extracted and combined into a matrix, i.e. raster, with rows representing electrodes and columns representing time steps. A population time vector was obtained by summing nLFPs in the raster for each time step, and avalanches were defined as spatiotemporal continuous activity in the population vector bracketed by at least one time-bin with no activity. The size of an avalanche, S, was defined as the number of nLFPs participating in the cascade. Multiple nLFPs at an electrode during an avalanche are rare (Yu et al., 2014) and were counted in size estimates. Scale invariance of S was visualized by plotting probability distributions P(S) in double-log coordinates. Given the difficulty of obtaining robust lifetime distributions in the presence of ongoing oscillations, the present work relied mainly on the calculation of size distributions and temporal profile collapse (for details see Miller, 2019 #45}.

Avalanche temporal profile collapse and scaling exponent. The avalanche lifetime, L, was defined by the number of timesteps that the avalanche persisted, and the temporal profile, S(t), was described by the number of participating electrodes at each timestep t = 1 … L. Avalanches were grouped by L in multiples of Δt and averaged to obtain the average temporal profile for a given lifetime, ⟨S⟩(t, L). Normalized to dimensionless time units, t/L, amplitudes were then rescaled via Equation 1.

$$\langle S\rangle\left(\frac{t}{L}\right) \sim L^{\chi-1}\ \boldsymbol{\mathcal{F}}\left(\frac{t}{L}\right) \tag{1}$$

The profile collapse function, shown in Equation 1, relates the mean profile for each lifetime L, ⟨S⟩(t/L), with a characteristic temporal motif $\boldsymbol{\mathcal{F}}$(t/L), and scaling factor, $L^{\chi-1}$, which is independent of L according to Equation 1. To perform a shape collapse, we plotted ⟨S⟩(t, L) from L-1 through L+1 for L_{min} = 3Δt (to reduce finite size effects in shape caused by too few data points) through L = L_{max} chosen based on the strength of our data set (>1,000 avalanches per *L*). The collapse error, Δ_F, was quantified via a normalized mean squared error (NMSE) of height-normalized individual profiles to the combined normalized average of all collapsed profiles, $\boldsymbol{\mathcal{F}}$(t/L). Minimized collapse error was calculated by scanning through χ = 0.5 to 3 at resolution of 0.001 to find the collapse in avalanche waveform associated with the smallest Δ_F via $\chi_{collapse}$. A value of $\Delta_F > 1$ was considered a failure in collapse.

Parabolic fit. For the parabolic fit we used the approach by (Laurson et al., 2013) as follows:

$$y = A \cdot \frac{t}{T}\left(1 - \frac{t}{T}\right)^{\gamma-0.5} \tag{2}$$

The parabolic fit error, Δ_{parab}, was quantified via a normalized mean squared error (NMSE) of individual profiles to an amplitude-matched parabola which was coarse-grained to match L. Comparison to a semicircle fit was conducted in the same manner to obtain Δ_{semi} using:

$$y = A \cdot \sqrt{1 - \left({}^{t}/_{T}\right)^{2}} \tag{3}$$

Avalanche statistical tests and slope estimates. The maximum log-likelihood ratio (LLR) was calculated to test potential power law distributions against the alternatives of exponential or log-normal distribution models (Clauset et al., 2009; Klaus et al., 2011). When tested positive for power law, the LLR estimate for best slope was reported. Here we used the range of S = 1 to 40, which excludes the distribution cut-off close to the total number of functional electrodes on the array (n = >70).

Normalized Count network reconstruction. To remove the influence of common input to electrodes on the array which inflates the Pearson's pairwise correlation, we conducted a network reconstruction. This nonparametric method, called the Normalized Count (NC) approach, is used for the network reconstruction because its computational efficiency is comparable to the correlation analysis but with much lower reconstruction error, which are important considerations for analysis of long LFP time series collected in awake *in vivo* preparations. For this reconstruction, the time-window within which active nodes can influence each other was examined for 0.5, 1, <IEI>, and 30 ms. For each node activation (spike), all nodes that were active within Δt, prior to the spike, were deemed as potential causes. Results were similar for Δt = 0.5 and 1 ms. For longer Δt, the precision of the algorithm decreases rapidly due to (1) the increase in ambiguous potential associations between the number of active nodes

in successive frames and (2) a decrease in frame transitions to estimate link weights (Pajevic and Plenz, 2009). Here we show results for $\Delta t = 1$ ms, which matches our avalanche scaling analysis.

Correlation based network reconstruction. Networks were reconstructed for each recording session individually and the links with low pairwise correlations were removed before subsequent network analysis. Rather than applying a strict minimum correlation threshold for removing the links, which would leave our analysis vulnerable to inter-subject differences in electrode impedances, etc., we instead sequentially removed the weakest links in 0.01 increments until a predefined sparsity of approximately 40% was achieved. Weight bins were divided into deciles for pruning analysis and quintiles for entropy analysis, for ease of visualization (Fig. 4, 5).

Integrative networks and Pruning analysis. Once the networks were defined, we studied their integrative properties (Pajevic and Plenz, 2012). The link clustering coefficient, C_L, was defined for each link as the ratio of the number of common neighbors of its end nodes to the number of all neighbors. In an integrative network, there is a positive correlation R_{CL} between C_L and the weight of the link, indicating that strongly connected nodes are likely to share more common neighbors. We also conducted a "pruning analysis" in which we studied the robustness of the excess node clustering ΔC upon the progressive removal of the weakest (bottom pruning) or strongest (top pruning) links. The excess node clustering was defined as the difference of the clustering coefficient of the original network and the corresponding randomized network, randomized using degree sequence preserved randomization (DSPR).

Network link mixing and entropy analysis. Link weights fluctuated over time in both pairwise correlation and directed causal networks. We wanted to explore whether these fluctuations

predominantly represent an error in network reconstruction or arise from a genuine and progressive change in network weights. To visualize and quantify the progression of these fluctuations in individual link strengths from one day to another, we stratify the links in two steps using the Day 1 data. In the first step we choose either 50% of the strongest links (top links), or 50% percent of the weakest links (bottom links) to conduct the entropy of mixing analysis. In a second step, the chosen half (either top or bottom) are labelled based on their magnitude, while the other half is removed from consideration. The labelling is done by sorting the chosen links by magnitude of their weights and partitioning them into a finite set of classes, N_c. In our case, we used $N_c = 5$, so that the label $c=1$ marked the weakest 20% of the sorted links and incrementally, c = 5 marked the strongest 20% of the links. Note that effectively the strongest 20% links are actually representing the 10% of strongest links in the full network, if the "top" half is used, while the weakest 20% of the "top" links have still greater magnitude than the strongest quintile of the "bottom". We then monitor the weights of the chosen links for subsequent days, which we now sort based on their new weights, but now partition them over a potentially larger number of weight groups, $N_g = k\, N_c$, where k is an integer, in order to make all groups contain a single label (initially we use k = 3 and $N_g = 15$). Due to (1) reconstruction errors and (2) potential actual network weight changes from one day to another, each of the groups will contain a mixture of the original labels, although it is expected that the low group indices, g, will early on predominantly carry the labels of the weak links. For each group, we calculate a fraction, f_c, of the links that carry label c, which by definition are normalized to 1, i.e., $\sum_{c=1}^{N_c} f_c = 1$. For each group g we then calculate the Shannon entropy of such mixture according to $H_g = -\sum_{c=1}^{N_c} f_c \log f_c$. In the end we report the average and the standard error over all non-

edge groups values of H_g, i.e., excluding the extreme bins, as those have only uni-directional mixing (n=N_g-2=13). Hence, our average entropy of mixing is $H_M = \frac{1}{N_g-2}\sum_{g=2}^{N_g-1} H_g$.

To evaluate if we have seen a progression in the weight evolution, we test it against the null hypothesis that there was no significant linear trend across the subsequent days. To do so we use a Monte Carlo (MC) procedure, in which we generate one million normally distributed replicates, N(0,σ_G) for each point, where σ_G are the standard deviations obtained using the non-edge groups, as described in the previous paragraph. For each of the N_{MC}=1000000 replicates we perform a linear regression and count the number of times the MC slopes were greater than the slope we obtained using the mean values for H_M. From this count, N_{pos}, our estimate of the p values is p=(N_{pos}+1)/(N_{MC}+1).

Acknowledgements

We thank members of the Plenz lab and attendees of the "*Critical brain dynamics: 5th International Workshop on Criticality and the Brain*", 2016, NIH, USA for their support and useful discussions.

Funding sources

This research was supported by the Intramural Research Program of the National Institute of Mental Health ZIAMH002797, USA to D.P. and the *Eunice Kennedy Shriver* National Institute of Child Health and Human Development to S.P. This research utilized the computational resources of the NIH HPC Biowulf cluster (http://hpc.nih.gov).

Author Contributions

S.Y. collected the data; S.R.M. , S.Y. and S.P. analyzed the data; S.R.M., S.Y., S.P. and D.P. wrote the manuscript.

Supplementary Information

No Supplementary Information.

Competing interests:

The authors declare no competing interests.

Tables

Table 1. Summary of average estimates for the mean Pearson's pairwise correlation coefficient, <R>, the exponent α of avalanche size distributions for each nonhuman primate and array at temporal resolutions of Δt = 1 ms and Δt = 30 ms respectively. Exponents were derived from maximum likelihood estimates. Stability of α over all recording days was quantified by the linear regression slope within 95% confidence limits (CL).

	<R> Stability	**Avalanche size distribution (Δt=1ms)**	**Exponent α stability (Δt=1ms)**	**Avalanche size distribution (Δt=<IEI>)**	**Exponent α stability (Δt=<IEI>)**	**Avalanche size distribution (Δt= 30 ms)**	**Exponent α stability (Δt=30 ms)**
	Regression slope (95% CL) ($x10^{-3}$)	Exponent α (± s.d.)	Regression slope (95% CL) ($x10^{-3}$)	Exponent α (± s.d.)	Regression slope (95% CL) ($x10^{-3}$)	Exponent α (± s.d.)	Regression slope (95% CL) ($x10^{-3}$)
V-PF	-1 (-3, 2)	1.71 ± 0.00	0 (-1, 0)	1.26 ± 0.01	-2 (-3, 3)	0.65 ± 0.03	-3 (-9, 2)
V-PM	0 (-62, 62)	1.64 ± 0.02	6 (-40, 51)	1.29 ± 0.04	16 (-28, 60)	1.12 ± 0.05	20 (-2, 43)
N-PF	1 (0, 2)	1.71 ± 0.02	-1 (-1, 0)	1.41 ± 0.01	0 (-1, 0)	0.97 ± 0.02	0 (-1, 1)
N-PM	1 (-13, 15)	1.73 ± 0.02	2 (-8, 12)	1.31 ± 0.02	0 (-1, 1)	0.75 ± 0.02	3 (-6, 12)
K-PF1	1 (0, 1)	1.65 ± 0.02	-1 (-1, 0)	1.29 ± 0.01	0 (-1, 0)	0.90 ± 0.02	0 (0, 1)
K-PF2	0 (-20, 20)	1.77 ± 0.03	5 (-33, 43)	1.36 ± 0.02	1 (-27, 29)	0.74 ± 0.03	10 (-16, 35)
mean ± sd	**0 ± 1**	**1.70 ± 0.05**	**2 ± 3**	**1.32 ± 0.05**	**3 ± 7**	**0.86 ± 0.17**	**5 ± 9**

Table 2. Summary of scaling function estimate for the temporal profile of neuronal avalanches. A parabolic fit is compared to a semicircle fit at temporal resolutions Δt = 1 ms and Δt = 30 ms for each nonhuman primate and array and its corresponding phase randomized profile (*random*) at Δt = 1 ms.

	Temporal Profile Fit: Parabola vs. Semicircle RMSE (Δt = 1ms)		**Temporal Profile Fit: Parabola vs. Semicircle RMSE (Δt = 30ms)**		**Random Profile Fit: Parabola vs. Semicircle RMSE (Δt = 1ms)**	
	Paired t-Test (p-value)	ANOVA (F)	Paired t-Test (p-value)	ANOVA (F)	Paired t-Test (p-value)	ANOVA (F)
V-PF	4.36E-05	110.44	2.00E-04	62.26	5.96E-10	4832.54
V-PM	3.87E-04	121.17	3.40E-05	417.07	7.82E-07	2776.65
N-PF	6.12E-11	460.49	2.66E-13	1156.15	3.74E-14	1607.96
N-PM	6.81E-08	991.66	3.15E-06	272.38	2.41E-10	6533.12
K-PF1	2.76E-22	472.2	2.41E-25	715.09	1.98E-50	18530.05
K-PF2	2.60E-06	290.68	9.64E-06	186.09	1.91E-09	3277.87
mean ± sd	**Par < Semi**	**Par < Semi**	**Par< Semi**	**Par < Semi**	**Par > Semi**	**Par > Semi**

Table 3. Summary of estimates for the scaling exponent χ to optimally collapse temporal avalanche profiles at temporal resolutions $\Delta t = 1$ ms and $\Delta t = 30$ ms for each nonhuman primate and array. The stability of χ over all recording days were quantified by the linear regression slope reported and 95% confidence limits. *Random*: Phase randomized control of temporal avalanche profile.

	Scaling Exponent χ (Δt = 1ms)	**χ Stability (Δt = 1ms)**	**Scaling Exponent χ (Δt = 30 ms)**	**χ Stability (Δt = 30ms)**	**Scaling Exponent χ Random (Δt = 1ms)**	**χ Stability Random (Δt = 1ms)**
	Mean χ (± s.d.)	Regression slope (95% CL)	Mean χ (± s.d.)	Regression slope (95% CL)	Mean χ (± s.d.)	Regression slope (95% CL)
V-PF	1.78 ± 0.05	0.002 (-0.019, 0.022)	1.61 ± 0.09	-0.01 (-0.02, 0.01)	1.15 ± 0.01	0.001 (-0.001, 0.003)
V-PM	1.93 ± 0.15	0.051 (-0.3, 0.4)	2.25 ± 0.20	0.06 (-0.6, 0.7)	1.15 ± 0.00	0.000 (-0.001, 0.002)
N-PF	2.10 ± 0.06	0.002 (-0.000, 0.004)	2.15 ± 0.15	-0.00 (-0.01, 0.00)	1.14 ± 0.03	0.000 (-0.001, 0.002)
N-PM	2.05 ± 0.13	0.011 (-0.053, 0.075)	1.85 ± 0.05	0.005 (-0.016, 0.027)	1.14 ± 0.01	0.002 (-0.005, 0.008)
K-PF1	1.92 ± 0.03	0.000 (-0.001, 0.001)	2.11 ± 0.1	-0.000 (-0.003, 0.003)	1.15 ± 0.01	0.000 (-0.000, 0.000)
K-PF2	1.76 ± 0.02	0.007 (-0.004, 0.018)	2.12 ± 0.20	0.086 (-0.029, 0.2)	1.15 ± 0.00	0.000 (-0.004, 0.005)
mean (± s.d.)	**1.93 ± 0.14**	**0.012 ± 0.19**	**2.01 ± 0.24**	**0.02 ± 0.04**	**1.15 ± 0.01**	**0.001 ± 0.001**

Table 4. Functional network stability based on NC reconstruction algorithm at $\Delta t = 1$. Shown is the stability of R_{CL} over time (see also Fig. 5D). H_M P values given for top 50% and bottom 50% for significant trend in mixing observed.

	R_{CL} Stability (Δt = 1 ms)	**H_M Trend (Δt = 1 ms)**	
	Regression slope (95% CL) ($\times 10^{-3}$)	top 50% *P*	Bottom 50% *P*
V-PF	-1 (-28, 18)	0.46	0.34
V-PM	0 (-62, 62)	0.007	0.05
N-PF	1 (0, 0.002)	$<10^{-5}$	0.03
N-PM	14 (-13, 15)	0.08	0.54
K-PF1	1 (0, 1)	0.003	0.2
K-PF2	0 (-20, 21)	0.27	0.35
mean (± s.d.)	**5 ± 10**		

References

Alstott, J., Pajevic, S., Bullmore, E., and Plenz, D. (2015). Opening bottlenecks on weighted networks by local adaptation to cascade failures. Journal of Complex Networks *3*, 552-565.

Barrat, A., Barthelemy, M., Pastor-Satorras, R., and Vespignani, A. (2004). The architecture of complex weighted networks. Proc Natl Acad Sci U S A *101*, 3747-3752.

Bassett, D.S., and Sporns, O. (2017). Network neuroscience. Nature Neuroscience *20*, 353-364.

Beggs, J.M., and Plenz, D. (2003). Neuronal avalanches in neocortical circuits. J Neurosci *23*, 11167-11177.

Bellay, T., Klaus, A., Seshadri, S., and Plenz, D. (2015). Irregular spiking of pyramidal neurons organizes as scale-invariant neuronal avalanches in the awake state. Elife *4*.

Bianconi, G. (2005). Emergence of weight-topology correlations in complex scale-free networks. Europhysics Letters *71*, 1029-1035.

Bullmore, E., and Sporns, O. (2009). Complex brain networks: graph theoretical analysis of structural and functional systems. NatRevNeurosci *10*, 186-198.

Chialvo, D.R., Cannas, S.A., Grigera, T.S., Martin, D.A., and Plenz, D. (2020). Controlling a complex system near its critical point via temporal correlations. Scientific Reports *10*, 12145.

Clauset, A., Shalizi, C.R., and Newman, M.E.J. (2009). Power-Law Distributions in Empirical Data. Siam Rev *51*, 661-703.

Deco, G., Kringelbach, M.L., Jirsa, V.K., and Ritter, P. (2017). The dynamics of resting fluctuations in the brain: metastability and its dynamical cortical core. Scientific Reports *7*, 3095.

Dickey, A.S., Suminski, A., Amit, Y., and Hatsopoulos, N.G. (2009). Single-unit stability using chronically implanted multielectrode arrays. Journal of neurophysiology *102*, 1331-1339.

Donoghue, J.P., Sanes, J.N., Hatsopoulos, N.G., and Gaál, G.n. (1998). Neural discharge and local field potential oscillations in primate motor cortex during voluntary movements. Journal of neurophysiology *79*, 159-173.

Fox, M.D., and Raichle, M.E. (2007). Spontaneous fluctuations in brain activity observed with functional magnetic resonance imaging. Nat Rev Neurosci *8*, 700-711.

Fraiman, D., and Chialvo, D.R. (2012). What kind of noise is brain noise: anomalous scaling behavior of the resting brain activity fluctuations. Front Physiol *3*.

Fraser, G.W., and Schwartz, A.B. (2011). Recording from the same neurons chronically in motor cortex. Journal of neurophysiology *107*, 1970-1978.

Friedman, N., Ito, S., Brinkman, B.A.W., Shimono, M., DeVille, R.E.L., Dahmen, K.A., Beggs, J.M., and Butler, T.C. (2012). Universal critical dynamics in high resolution neuronal avalanche data. Phys Rev Lett *108*, 208102.

Gautam, H., Hoang, T.T., McClanahan, K., Grady, S.K., and Shew, W.L. (2015). Maximizing Sensory Dynamic Range by Tuning the Cortical State to Criticality. Plos Comput Biol *11*.

Hansen, E.C.A., Battaglia, D., Spiegler, A., Deco, G., and Jirsa, V.K. (2015). Functional connectivity dynamics: Modeling the switching behavior of the resting state. Neuroimage *105*, 525-535.

Harris, T.E. (1963). The theory of branching processes (Berlin: Springer-Verlag).

Hutchison, R.M., Womelsdorf, T., Allen, E.A., Bandettini, P.A., Calhoun, V.D., Corbetta, M., Della Penna, S., Duyn, J.H., Glover, G.H., Gonzalez-Castillo, J.*, et al.* (2013). Dynamic functional connectivity: Promise, issues, and interpretations. NeuroImage *80*, 360-378.

Jackson, A., and Fetz, E.E. (2007). Compact Movable Microwire Array for Long-Term Chronic Unit Recording in Cerebral Cortex of Primates. Journal of Neurophysiology *98*, 3109-3118.

Kinouchi, O., and Copelli, M. (2006). Optimal dynamical range of excitable networks at criticality. Nat Phys *2*, 348-352.

Klaus, A., Yu, S., and Plenz, D. (2011). Statistical Analyses Support Power Law Distributions Found in Neuronal Avalanches. Plos One *6*.

Laurson, L., Illa, X., Santucci, S., Tore Tallakstad, K., Måløy, K.J., and Alava, M.J. (2013). Evolution of the average avalanche shape with the universality class. Nature Communications *4*, 2927.

Levina, A., and Priesemann, V. (2017). Subsampling scaling. Nature Communications *8*, 15140.

Li, M., Liu, F., Jiang, H., Lee, T.S., and Tang, S. (2017). Long-Term Two-Photon Imaging in Awake Macaque Monkey. Neuron *93*, 1049-1057.e1043.

Liu, X., and Duyn, J.H. (2013). Time-varying functional network information extracted from brief instances of spontaneous brain activity. Proceedings of the National Academy of Sciences *110*, 4392-4397.

Lutcke, H., Margolis, D.J., and Helmchen, F. (2013). Steady or changing? Long-term monitoring of neuronal population activity. Trends Neurosci *36*, 375-384.

Ma, Z., Turrigiano, G.G., Wessel, R., and Hengen, K.B. (2019). Cortical Circuit Dynamics Are Homeostatically Tuned to Criticality In Vivo. Neuron.

Mehring, C., Rickert, J., Vaadia, E., Cardosa, d.O., Aertsen, A., and Rotter, S. (2003). Inference of hand movements from local field potentials in monkey motor cortex. Nat Neurosci *6*, 1253-1254.

Meisel, C., Olbrich, E., Shriki, O., and Achermann, P. (2013). Fading Signatures of Critical Brain Dynamics during Sustained Wakefulness in Humans. J Neurosci *33*, 17363-17372.

Miller, S.R., Yu, S., and Plenz, D. (2019). The scale-invariant, temporal profile of neuronal avalanches in relation to cortical γ–oscillations. Scientific Reports *9*, 16403.

Nicolelis, M.A., Dimitrov, D., Carmena, J.M., Crist, R., Lehew, G., Kralik, J.D., and Wise, S.P. (2003). Chronic, multisite, multielectrode recordings in macaque monkeys. ProcNatlAcadSciUSA *100*, 11041-11046.

Onnela, J.P., Saramaki, J., Hyvonen, J., Szabo, G., Lazer, D., Kaski, K., Kertesz, J., and Barabási, A.L. (2007). Structure and tie strengths in mobile communication networks. ProcNatlAcadSciUSA *104*, 7332-7336.

Pajevic, S., and Plenz, D. (2009). Efficient Network Reconstruction from Dynamical Cascades Identifies Small-World Topology of Neuronal Avalanches. Plos Comput Biol *5*.

Pajevic, S., and Plenz, D. (2012). The organization of strong links in complex networks. Nat Phys *8*, 429-436.

Petermann, T., Thiagarajan, T., Lebedev, M.A., Nicolelis, M.A., Chialvo, D.R., and Plenz, D. (2009). Spontaneous cortical activity in awake monkeys composed of neuronal avalanches. Proc Natl Acad Sci U S A *106*, 15921-15926.

Plenz, D. (2012). Neuronal avalanches and coherence potentials. The European Physical Journal Special Topics *205*, 259-301.

Ponce-Alvarez, A., Jouary, A., Deco, G., and Sumbre, G. (2018). Whole brain neuronal activtity displays crackling noise dynamics. (reviewed for neuron).

Raichle, M.E. (2015). The Brain's Default Mode Network. Annual Review of Neuroscience *38*, 433-447.

Rasch, M.J., Gretton, A., Murayama, Y., Maass, W., and Logothetis, N.K. (2008). Inferring spike trains from local field potentials. J Neurophysiol *99*, 1461-1476.

Ribeiro, T.L., Copelli, M., Caixeta, F., Belchior, H., Chialvo, D.R., Nicolelis, M.A., and Ribeiro, S. (2010). Spike avalanches exhibit universal dynamics across the sleep-wake cycle. Plos One *5*, e14129.

Ribeiro, T.L., Ribeiro, S., Belchior, H., Caixeta, F., and Copelli, M. (2014). Undersampled Critical Branching Processes on Small-World and Random Networks Fail to Reproduce the Statistics of Spike Avalanches. Plos One *9*, e94992.

Sethna, J.P., Dahmen, K.A., and Myers, C.R. (2001). Crackling noise. Nature *410*, 242-250.

Shew, W.L., Yang, H.D., Petermann, T., Roy, R., and Plenz, D. (2009). Neuronal Avalanches Imply Maximum Dynamic Range in Cortical Networks at Criticality. J Neurosci *29*, 15595-15600.

Shew, W.L., Yang, H.D., Yu, S., Roy, R., and Plenz, D. (2011). Information Capacity and Transmission Are Maximized in Balanced Cortical Networks with Neuronal Avalanches. J Neurosci *31*, 55-63.

Shriki, O., Alstott, J., Carver, F., Holroyd, T., Henson, R.N.A., Smith, M.L., Coppola, R., Bullmore, E.T., and Plenz, D. (2013). Neuronal Avalanches in the Resting MEG of the Human Brain. J Neurosci *33*, 7079-7090.

Stewart, C.V., and Plenz, D. (2008). Homeostasis of neuronal avalanches during postnatal cortex development in vitro. J Neurosci Meth *169*, 405-416.

Tagliazucchi, E., Balenzuela, P., Fraiman, D., and Chialvo, D.R. (2012). Criticality in large-scale brain fMRI dynamics unveiled by a novel point process analysis. Front Physiol *3*.

Tetzlaff, C., Okujeni, S., Egert, U., Worgotter, F., and Butz, M. (2010). Self-Organized Criticality in Developing Neuronal Networks. Plos Comput Biol *6*.

Tolias, A.S., Ecker, A.S., Siapas, A.G., Hoenselaar, A., Keliris, G.A., and Logothetis, N.K. (2007). Recording chronically from the same neurons in awake, behaving primates. Journal of neurophysiology *98*, 3780-3790.

Villegas, P., Di Santo, S., Burioni, R., and Muñoz, M.A. (2019). Time-series thresholding and the definition of avalanche size. Phys Rev E *100*.

Yang, H.D., Shew, W.L., Roy, R., and Plenz, D. (2012). Maximal Variability of Phase Synchrony in Cortical Networks with Neuronal Avalanches. J Neurosci *32*, 1061-1072.

Yu, S., Klaus, A., Yang, H.D., and Plenz, D. (2014). Scale-Invariant Neuronal Avalanche Dynamics and the Cut-Off in Size Distributions. Plos One *9*.

Yu, S., Ribeiro, T.L., Meisel, C., Chou, S., Mitz, A., Saunders, R., and Plenz, D. (2017). Maintained avalanche dynamics during task-induced changes of neuronal activity in nonhuman primates. Elife *6*.

Yu, S., Yang, H.D., Nakahara, H., Santos, G.S., Nikolic, D., and Plenz, D. (2011). Higher-Order Interactions Characterized in Cortical Activity. J Neurosci *31*, 17514-17526.

Zalesky, A., Fornito, A., Cocchi, L., Gollo, L.L., and Breakspear, M. (2014). Time-resolved resting-state brain networks. Proceedings of the National Academy of Sciences *111*, 10341.